

GEOLOGY

Multiple episodes of extensive marine anoxia linked to global warming and continental weathering following the latest Permian mass extinction

Feifei Zhang,^{1*} Stephen J. Romaniello,¹ Thomas J. Algeo,^{2,3} Kimberly V. Lau,⁴ Matthew E. Clapham,⁵ Sylvain Richoz,^{6,7} Achim D. Herrmann,⁸ Harrison Smith,¹ Micha Horacek,^{6,9,10} Ariel D. Anbar^{1,11}

Explaining the ~5-million-year delay in marine biotic recovery following the latest Permian mass extinction, the largest biotic crisis of the Phanerozoic, is a fundamental challenge for both geological and biological sciences. Ocean redox perturbations may have played a critical role in this delayed recovery. However, the lack of quantitative constraints on the details of Early Triassic oceanic anoxia (for example, time, duration, and extent) leaves the links between oceanic conditions and the delayed biotic recovery ambiguous. We report high-resolution U-isotope ($\delta^{238}\text{U}$) data from carbonates of the uppermost Permian to lowermost Middle Triassic Zal section (Iran) to characterize the timing and global extent of ocean redox variation during the Early Triassic. Our $\delta^{238}\text{U}$ record reveals multiple negative shifts during the Early Triassic. Isotope mass-balance modeling suggests that the global area of anoxic seafloor expanded substantially in the Early Triassic, peaking during the latest Permian to mid-Griesbachian, the late Griesbachian to mid-Dienerian, the Smithian-Spathian transition, and the Early/Middle Triassic transition. Comparisons of the U-, C-, and Sr-isotope records with a modeled seawater PO_4^{3-} concentration curve for the Early Triassic suggest that elevated marine productivity and enhanced oceanic stratification were likely the immediate causes of expanded oceanic anoxia. The patterns of redox variation documented by the U-isotope record show a good first-order correspondence to peaks in ammonoid extinctions during the Early Triassic. Our results indicate that multiple oscillations in oceanic anoxia modulated the recovery of marine ecosystems following the latest Permian mass extinction.

INTRODUCTION

The 252-million-year-old Permian-Triassic boundary (PTB) mass extinction represents the largest biotic crisis in Earth's history (1), during which ~90% of marine and ~75% of terrestrial species went extinct over ~61(\pm 48) thousand years (ka) (1, 2). The Early Triassic was an interval of protracted marine biotic recovery (1, 3, 4). An initial, aborted recovery occurred soon after the latest Permian mass extinction (LPME) crisis, during the Induan stage of the Early Triassic (1, 5, 6), and a more sustained recovery took place during the late Olenekian stage (Spathian substage) (1, 7–9); however, full marine ecosystem recovery did not occur until the Middle Triassic, 4 to 8 million years (Ma) after the LPME (1). This delay has been attributed to various causes, including the intensity of the PTB extinction event (10), persistently high temperatures (11), productivity crises (12), and/or episodically recurring environmental perturbations (13–16).

Although the mechanisms for the long duration of the post-LPME recovery are debated, marine anoxia has been invoked in many studies

(3, 4, 17–21). Ce anomalies and Th/U ratios in conodont apatite were used to reconstruct a 20-Ma redox history from the latest Permian to Late Triassic, revealing anoxic events during the late Changhsingian-Griesbachian, Smithian-Spathian transition, and the mid-Spathian (19). Mo/Al ratios and the pyrite content of mudstones on the continental slope of the eastern Panthalassic margin were used to infer euxinic conditions during the late Changhsingian to mid-Dienerian and mid-Smithian to mid-Spathian intervals (20). Fe speciation was used to demonstrate a dynamic redox history along the Oman margin, with an expanded oxygen-minimum zone during the late Changhsingian to earliest Griesbachian, the Dienerian-Smithian transition, and the Smithian-Spathian transition (21). However, these proxies are inherently local in terms of their paleoredox implications, and high-resolution changes in mean global-ocean redox conditions during the Early Triassic remain poorly constrained despite their likely importance for understanding links between oceanic conditions and the delayed marine biotic recovery.

The present study addresses this gap in knowledge regarding Early Triassic oceanic redox conditions through analysis of a global-ocean redox proxy, the U isotopes in marine carbonates ($^{238}\text{U}/^{235}\text{U}$, denoted as $\delta^{238}\text{U}$) (18, 22–25). Because of the long residence time of U in the ocean (~500 ka) (26), seawater U is well-mixed and exhibits globally uniform concentrations (3.14 to 3.59 $\mu\text{g}/\text{liter}$) (26) and isotopic compositions [ca. -0.39‰ (per mil)] (27–29). Seawater $\delta^{238}\text{U}$ will tend to remain well-mixed even when the extent of oceanic oxygenation is significantly lower than today (25). Variations in the U-isotope compositions of primary carbonate precipitates (such as scleractinian corals, calcareous green and red algae, ooids, and mollusks) are thought to track the $\delta^{238}\text{U}$ of contemporaneous seawater (24).

¹School of Earth and Space Exploration, Arizona State University, Tempe, AZ 85287–6004, USA. ²Department of Geology, University of Cincinnati, Cincinnati, OH 45221–0013, USA. ³State Key Laboratories of Biogeology and Environmental Geology and Geological Processes and Mineral Resources, China University of Geosciences, Wuhan 430074, China. ⁴Department of Earth Sciences, University of California, Riverside, Riverside, CA 92521, USA. ⁵Department of Earth and Planetary Sciences, University of California, Santa Cruz, Santa Cruz, CA 95064, USA. ⁶Institute of Earth Sciences, NAWI Graz, University of Graz, Heinrichstraße 26, 8010 Graz, Austria. ⁷Department of Geology, Lund University, Sölvegatan 12, 22362 Lund, Sweden. ⁸Department of Geology and Geophysics, Louisiana State University, Baton Rouge, LA 70803, USA. ⁹Lehr- und Forschungszentrum Francisco-Josephinum, 3250 Wieselburg, Austria. ¹⁰Department of Lithospheric Research, Vienna University, Althanstr. 14, 1090 Vienna, Austria. ¹¹School of Molecular Sciences, Arizona State University, Tempe, AZ, 85287, USA.

*Corresponding author. Email: fzhang48@asu.edu

The U-isotope composition of seawater depends on redox conditions of the global ocean because U isotopes undergo different amounts of isotopic fractionation during incorporation into oxic and anoxic depositional facies. The largest source of U to the ocean is weathering from the upper continental crust and transport of dissolved U(VI) to the oceans via rivers. The $\delta^{238}\text{U}$ of rivers ranges from -0.18 to -0.38‰ , with a mean of -0.26‰ (30), which is slightly higher than the $\delta^{238}\text{U}$ of seawater (-0.39‰) (29). There are multiple sinks for seawater U, of which biogenic carbonates, sediments in anoxic facies, and sediments in weakly oxygenated facies, represent the bulk of U removal from the ocean, whereas the adsorption to Fe and Mn oxides and the hydrothermal alteration of oceanic crust represent smaller sinks (29, 31). Removal of U(IV) to anoxic sediments favors the ^{238}U isotope and is associated with an average fractionation ($\Delta^{238}\text{U}$) of $+0.6\text{‰}$, based on observations from the modern Black Sea, Kyllaren Fjord, and Saanich Inlet (27, 32–34). Removal of U under suboxic conditions (that is, corresponding to the integrated $\text{NO}_3\text{-Fe-Mn}$ reduction zones) favors ^{238}U with a fractionation factor of ca. $+0.1\text{‰}$, based on observations from the Peru Margin, where sediments underlying weakly oxygenated waters have an average $\delta^{238}\text{U}$ of $-0.28 (\pm 0.19)\text{‰}$ (27). Therefore, seawater is expected to have lower $\delta^{238}\text{U}$ at times of expanded oceanic anoxia and higher $\delta^{238}\text{U}$ at times of enhanced oceanic oxygenation (18, 22, 27, 35).

The $\delta^{238}\text{U}$ of primary marine carbonate precipitates reflects that of the seawater from which they precipitate (24, 27, 28). These natural observations are supported by laboratory experiments that suggest a negligible to small offset ($<0.13\text{‰}$) between primary carbonate and seawater $\delta^{238}\text{U}$ (36). However, sedimentary carbonates may incorporate U(IV) from sulfidic porewaters, leading to $\delta^{238}\text{U}$ values that are 0.2 to 0.4‰ higher than that of seawater (discussed further below and in the Supplementary Materials) (24). Thus, provided care is taken to correct for possible diagenetic alteration, U isotopes in ancient marine carbonates can serve as a global-ocean paleoredox proxy.

To date, four published studies have examined U-isotope variation during the Permian-Triassic transition and its aftermath (18, 22, 23, 25). Brennecke *et al.* (22) analyzed the narrow PTB interval at Dawen, South China, and documented a rapid expansion of oceanic anoxia across the LPME. This pattern was subsequently confirmed by Lau *et al.* (18) and Elrick *et al.* (23) in Tethys sections, and by Zhang *et al.* (25), who confirmed the same trend for a Panthalassic section. Together, these studies confirm the global nature of this event and the overall reliability of contemporaneous carbonate $\delta^{238}\text{U}$ records from widely spaced sections. Lau *et al.* (18) provided evidence for widespread oceanic anoxia from the latest Permian until the early Middle Triassic. However, although Lau *et al.* (18) provided evidence supporting the role of oceanic anoxia in the delayed recovery of marine ecosystems following the LPME, the resolution of this study was insufficient for the recognition of high-frequency redox fluctuations during the first ~ 2 Ma of the Early Triassic, an interval characterized by large $\delta^{13}\text{C}$ excursions ranging from -3 to $+8\text{‰}$ (3). Here, we provide a high-resolution U-isotope record spanning the uppermost Permian to the lowermost Middle Triassic at Zal, Iran, to investigate the secular variation in global-ocean redox conditions and its connection to the delayed recovery of marine ecosystems during the Early Triassic.

MATERIALS AND METHODS

We measured U isotopes ($\delta^{238}\text{U}$) in well-preserved Permian-Triassic marine carbonates from Zal, Iran, which were deposited on a peri-

equatorial carbonate ramp at the margin of a microcontinent in the west-central Tethys Ocean (Fig. 1A). This site accumulated mainly limestones until the late Early Triassic and mainly dolostones thereafter (Fig. 1B; see Supplementary Materials for details of the study section). The Zal section accumulated in a well-aerated deep shelf environment below wave base (15, 37), at estimated water depths of 100 to 200 m during the late Permian and 50 to 100 m during the Griesbachian. Further shallowing yielded a high-energy shelf environment characterized by oolitic and oncoidal facies by the late Early Triassic (15). The Zal study section has a well-developed lithostratigraphic, biostratigraphic, $\delta^{13}\text{C}_{\text{carb}}$, and $^{87}\text{Sr}/^{86}\text{Sr}$ chemostratigraphic framework (15, 37, 38).

We analyzed a total of 155 carbonate samples for U isotopes. For each sample, ~ 3 g of powder was dissolved in 1 M hydrochloric acid (HCl). The resulting supernatant was spiked using a double spike containing ^{236}U and ^{233}U , and the spiked U was purified using chromatography methods as described by Zhang *et al.* (25). The $^{238}\text{U}/^{235}\text{U}$ values were determined with a ThermoFinnigan Neptune MC-ICP-MS instrument at Arizona State University (ASU) (W.M. Keck Laboratory for Environmental Biogeochemistry). The U isotopic compositions of samples are reported relative to those of CRM145 standard (whose $\delta^{238}\text{U}$ value is identical to those of CRM 112a and SRM 950a, other commonly used standards). The analytical precision of this method is better than $\pm 0.08\text{‰}$ (all uncertainties reported here are 2 SD; see the Supplementary Materials for additional method details).

RESULTS AND DISCUSSION

Multiple episodes of expanded oceanic anoxia during the Early Triassic

Marine carbonate sediments can faithfully record chemical signatures of seawater provided that postdepositional processes and detrital contamination do not cause significant alteration. These processes likely did not confound the U-isotope pattern across the LPME observed in the Zal section because this pattern agrees with those at Dawen, Dajiang, and Daxiakou, China, which were located on the eastern side of the Paleo-Tethys Ocean (18, 22, 23); at Kamura, which was deposited in the open Panthalassic Ocean (25); and at Taşkent, Turkey, which was located northwest of Zal, on the western margin of the Paleo-Tethys Ocean (18). The fact that these six paleogeographically widely separated PTB sections exhibit a similar negative shift of $\delta^{238}\text{U}$ at the LPME supports the use of carbonate U isotopes as a paleoredox proxy for the Early Triassic global ocean (see the Supplementary Materials for a compilation of $\delta^{238}\text{U}$ studies across PTB) (18, 22, 23).

Confidence in this conclusion is enhanced by examining trace element compositions (Al, Mn, and Sr) and elemental ratios (Mn/Sr and Rb/Sr) as indicators of sedimentary diagenesis (fig. S1 and table S1). In most of the study samples, these elemental tracers are consistent with the well-preserved marine carbonate, with little influence from detrital components, and cross-plots of $\delta^{238}\text{U}$ versus these tracers show no evidence of diagenetic alteration (figs. S2 to S6). Carbonate diagenesis models predict that the $\delta^{238}\text{U}$ signal is more robust than the $^{87}\text{Sr}/^{86}\text{Sr}$ signal with respect to secondary alteration (35). $^{87}\text{Sr}/^{86}\text{Sr}$ values from Zal carbonates show good agreement with other records of Early Triassic seawater $^{87}\text{Sr}/^{86}\text{Sr}$ (38, 39), which suggests that the primary seawater $\delta^{238}\text{U}$ signal may also be well-preserved. We adopted $\text{Mn}/\text{Sr} < 2.5$ as a diagenetic alteration threshold [after (40)], with 127 out of the 155 study samples meeting this criterion (see the Supplementary Materials for evidence of primary $\delta^{238}\text{U}$ values). Only those

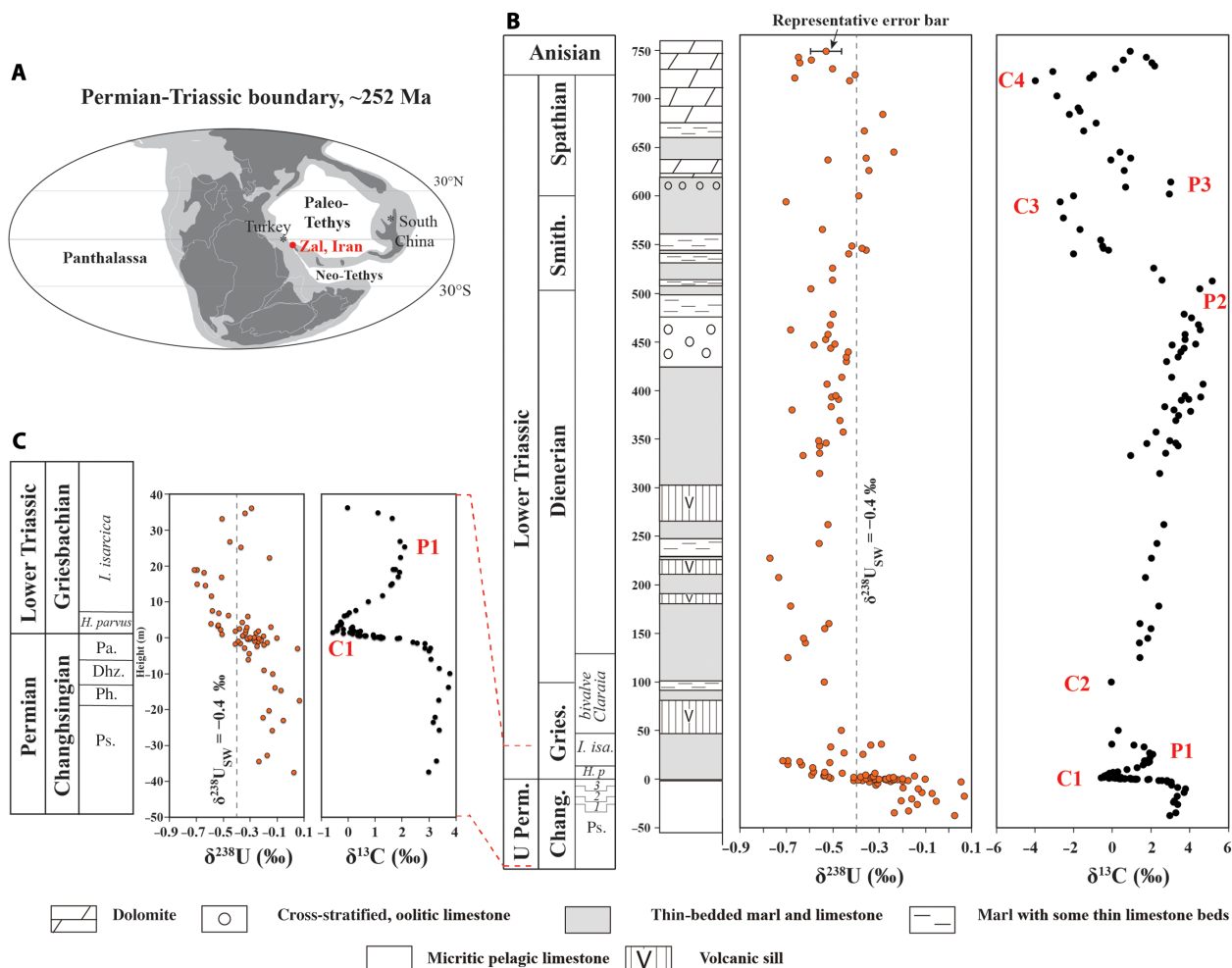


Fig. 1. Location of Iran at ~252 Ma ago and geochemical profiles for the Zal section. Paleogeographic location of Iran at ~252 Ma [(A) modified after the study of Payne *et al.* (60)] and geochemical profiles for Zal, Iran (B and C). The $^{238}\text{U}/^{235}\text{U}$ ratios are reported in per mil using standard δ -notation, where $\delta^{238}\text{U} = [(^{238}\text{U}/^{235}\text{U})_{\text{sample}} / (^{238}\text{U}/^{235}\text{U})_{\text{standard(CRM145)}} - 1] \times 1000$. $\delta^{13}\text{C}$ data and stratigraphic column are from Horacek *et al.* (15) and Richoz *et al.* (37). With respect to the $\delta^{13}\text{C}$ profile, C1 to C4 are equivalent to the N1 to N4 negative excursions of Song *et al.* (19). $\delta^{238}\text{U}_{\text{SW}}$ in (B) and (C) denotes $\delta^{238}\text{U}$ of modern seawater. A representative uncertainty range of 2 SD is shown for the uppermost $\delta^{238}\text{U}$ data point in (B). (C) Expanded view of the -40- to 40-m interval. Only samples with Mn/Sr < 2.5 are shown. Chang., Changhsingian; Gries., Griesbachian; Smith., Smithian. Following the studies of Clarkson *et al.* (21) and Martin *et al.* (44), biozonation of the Zal section is based on ammonoids for the Upper Permian and conodonts for the Lower Triassic. *I. isa.*, *Isarcicella isarcica*; *H. p.*, *Hindeodus parvus*; ammonoid zone 3, Pa., Paratirolites; ammonoid zone 2, Dhz., Dhzulfites; ammonoid zone 1, Ph., Phisonites; Ps., Pseudotoceras.

samples with Mn/Sr < 2.5 are plotted in Fig. 1 and used in the discussion below.

The $\delta^{238}\text{U}$ profile for Zal shows scatter of 0.2 to 0.4‰ through the Permian-Triassic transition interval, similar to that seen in sub-recent Bahamian carbonates. Although Bahamian primary carbonate precipitates appear to directly record seawater $\delta^{238}\text{U}$, all shallowly buried sediments have $\delta^{238}\text{U}$ that is isotopically heavier by 0.2 to 0.4‰ (mean, 0.3‰) than $\delta^{238}\text{U}$ of modern seawater (24). This is thought to reflect the differential incorporation of ^{238}U -enriched U(IV) from anoxic porewaters during early diagenesis or the variation in porewater U speciation during carbonate recrystallization (36). Porewater data from deep Bahamian drill cores suggest that the potential for alteration following burial may be limited because porewater anoxia renders U essentially immobile (41). On this basis, we have applied a diagenetic correction factor of 0.3‰ to measured $\delta^{238}\text{U}$ values before U-isotope mass-balance calculations (see the Supplementary Materials for further discussion).

The PTB interval at Zal is characterized by a large (3.5‰) and globally recognized negative $\delta^{13}\text{C}$ excursion commencing immediately before the LPME horizon (Fig. 1C, labeled “C1”) (37). A negative shift in $\delta^{238}\text{U}$ of ~0.4‰ commenced shortly below the LPME horizon (fig. S8; see the Supplementary Materials for discussion of timing of onset of oceanic anoxia). The shift toward lower carbonate $\delta^{238}\text{U}$ values in association with the extinction event is most readily interpreted as an increase in the flux of isotopically heavy U into anoxic facies, suggesting a rapid increase in the global area of anoxic seafloor in conjunction with the LPME event (18, 22, 23).

The high-resolution $\delta^{238}\text{U}$ data set presented here demonstrates that the Early Triassic ocean was characterized by multiple episodes of expanded anoxia. The negative $\delta^{238}\text{U}$ shift commencing shortly before the LPME reached a minimum of $-0.62 \pm 0.15\text{‰}$ about 15 m above the PTB (Fig. 1B). Low $\delta^{238}\text{U}$ values persisted through the Griesbachian substage, reaching a second, larger negative peak ($-0.73 \pm 0.09\text{‰}$) about

220 to 230 m above the PTB. This late Griesbachian to early Dienerian $\delta^{238}\text{U}$ minimum suggests that the most reducing conditions in the global ocean may have developed following the LPME crisis. The $\delta^{238}\text{U}$ values then gradually shift toward higher values, from ~230 to 550 m, recording a reduction under anoxic conditions during the mid-Dienerian to mid-Smithian. A third negative peak may be present at ~600 m based on a sample close to the Smithian-Spathian boundary, with a $\delta^{238}\text{U}$ of -0.70% , although more data are needed to confirm the existence of this feature. These values suggest widely reducing oceanic conditions throughout the Griesbachian to Smithian, with periodic fluctuations in areal extent. The top of the Zal section (700 to 752 m) shows a fourth negative $\delta^{238}\text{U}$ shift ($-0.57 \pm 0.19\%$), recording a major anoxic event during the latest Spathian to Early/Middle Triassic transition that is poorly known to date. Earlier U-isotope studies of Lower Triassic sections (18, 22, 23) did not delineate these multiple negative $\delta^{238}\text{U}$ shifts because of either insufficient stratigraphic coverage or insufficient temporal resolution. We predict that they will be observed in other coeval sections, and we encourage high-resolution $\delta^{238}\text{U}$ studies to reproduce these excursions.

Oceanic anoxia linked to climatic warming and marine nutrient levels

The U-isotope data set of the present study was generated using the same set of samples reported in earlier studies of $\delta^{13}\text{C}$ and $^{87}\text{Sr}/^{86}\text{Sr}$ at Zal (Fig. 2, A to C) (15, 38), allowing for direct comparisons among these records. All three isotopic records exhibit a series of four correlative excursions, during each of which negative excursions in $\delta^{238}\text{U}$ and $\delta^{13}\text{C}$ were accompanied by an accelerated rate of increase in $^{87}\text{Sr}/^{86}\text{Sr}$ (see the Supplementary Materials for a detailed comparison of LOWESS curves). The C1 event, which is latest Changhsingian to earliest Griesbachian in age, represents the well-documented marine environmental response to the LPME (11, 22, 25, 42, 43). The C2 event, which is latest Griesbachian to earliest Dienerian in age, exhibits U- and C-isotope minima that are similar to those of the C1 event, although the magnitudes of the excursions are smaller due to more negative initial values (Fig. 2). The C3 event, which is mid- to late Smithian in age, is well defined in the C- and Sr-isotope records, but more data are needed to fully test the duration and magnitude of a coeval U-isotope shift. The C4 event, which is latest Spathian to earliest Anisian in age, is characterized by smaller and more protracted $\delta^{238}\text{U}$ and $\delta^{13}\text{C}$ excursions than for the earlier events and by no apparent change in $^{87}\text{Sr}/^{86}\text{Sr}$ (although the existing Sr-isotope data set is too limited to adequately test for the C4 event) (Fig. 2, A to C). Although the patterns of excursions (for example, amplitude and duration) in the $\delta^{238}\text{U}$, $\delta^{13}\text{C}$, and $^{87}\text{Sr}/^{86}\text{Sr}$ profiles vary from one event to the next, the episodic nature of these events points to repeated global-scale perturbations that must have had significant impacts on global climate, weathering, and ocean redox dynamics.

The relationships between the $\delta^{238}\text{U}$, $\delta^{13}\text{C}$, and $^{87}\text{Sr}/^{86}\text{Sr}$ profiles for the Zal section were investigated through cross-correlation analysis of LOWESS-smoothed curves for each record (Fig. 2, A to C) (see the Supplementary Materials for a detailed discussion of cross-correlation methods). This analysis indicates that the negative shifts in $\delta^{238}\text{U}$ lagged behind the negative $\delta^{13}\text{C}$ excursions and the stepwise increases in the $^{87}\text{Sr}/^{86}\text{Sr}$ profile by 125 to 150 ka and 175 to 200 ka, respectively, and that the negative shifts in $\delta^{13}\text{C}$ lagged behind the stepwise increases in the $^{87}\text{Sr}/^{86}\text{Sr}$ profile by 0 to 50 ka. These lags are presumed to reflect differences in the residence times (and thus the relative response times) of seawater U, dissolved inorganic carbon, and Sr in Early Triassic oceans. Although each transient stepwise increase in the $^{87}\text{Sr}/^{86}\text{Sr}$

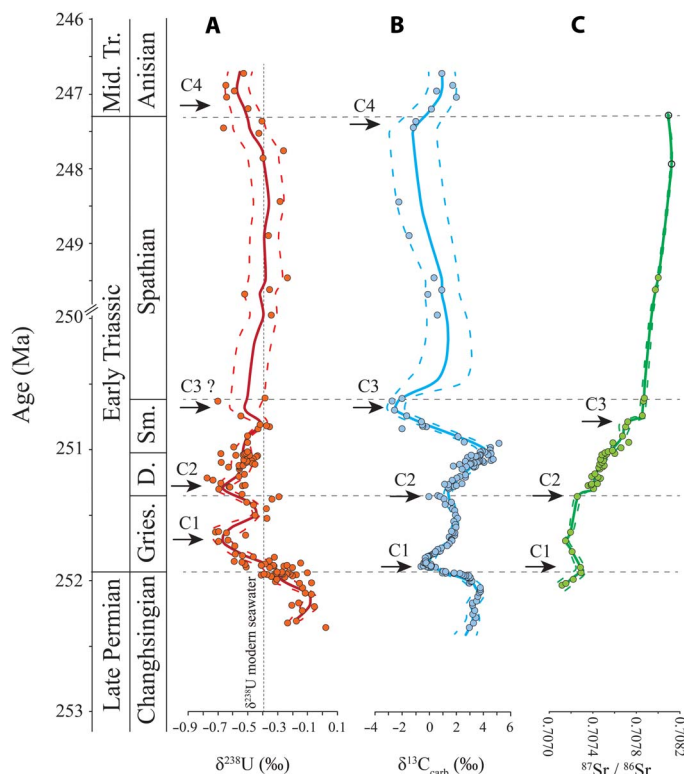


Fig. 2. LOWESS curves for $\delta^{238}\text{U}$, $\delta^{13}\text{C}$, and $^{87}\text{Sr}/^{86}\text{Sr}$ profiles of Zal, Iran. (A) Uranium isotope ($\delta^{238}\text{U}$) profile. (B) Carbon isotope ($\delta^{13}\text{C}$) profile (15, 37). $\delta^{13}\text{C}$ of samples without paired $\delta^{238}\text{U}$ data are not shown in this figure. (C) Strontium isotope ($^{87}\text{Sr}/^{86}\text{Sr}$) profile (38). U-C-Sr isotopes were measured from the same suite of samples. Samples with $\text{Mn}/\text{Sr} > 2.5$ have been removed from (A) and (B), and samples with $\text{Mn}/\text{Sr} > 2.5$ are indicated with open circles in (C). U. Perm., Upper Permian; Mid. Tr., Middle Triassic; Gries., Griesbachian; Di., Dienerian; Sm., Smithian. Note the change in time scale at 250 Ma.

profile was significantly shorter than the residence time of ~3 Ma for Sr in the modern ocean, the observed pattern could have been generated by a rapid pulsed injection of old radiogenic (that is, ^{87}Sr -enriched) Sr into the ocean system on time scales much shorter than the residence time of Sr. Similar effects have been reported from glacial-interglacial (~100 ka) cycles of the Quaternary (44, 45).

We hypothesize that these isotopic records were linked via a combination of enhanced volcanism and climatic warming, leading to increased crustal weathering and seawater PO_4^{3-} concentrations. Concurrent rapid warming and increases in seawater nutrient inventories would have led to oceanic anoxia as a result of increased marine primary productivity, reduced oxygen solubility, and reduced vertical mixing due to steeper thermal gradients in the oceanic thermocline.

Sr-isotope paleoweathering and O-isotope paleotemperature records suggest a general causal connection between climate warming and elevated weathering rates during the Early Triassic (11, 38). The increase in seawater $^{87}\text{Sr}/^{86}\text{Sr}$ from the latest Permian to the Early/Middle Triassic boundary occurred in a series of steps. Because each step is short, these events must represent large transient increases in the delivery of ^{87}Sr -rich weathering products to the ocean (38). Rising seawater $^{87}\text{Sr}/^{86}\text{Sr}$ could not have resulted from weathering of fresh basalts from the Siberian Traps (43) but rather, must have included a large contribution from weathering of old continental rocks with high $^{87}\text{Sr}/^{86}\text{Sr}$ ratios. $^{87}\text{Sr}/^{86}\text{Sr}$ records and sedimentary flux investigations

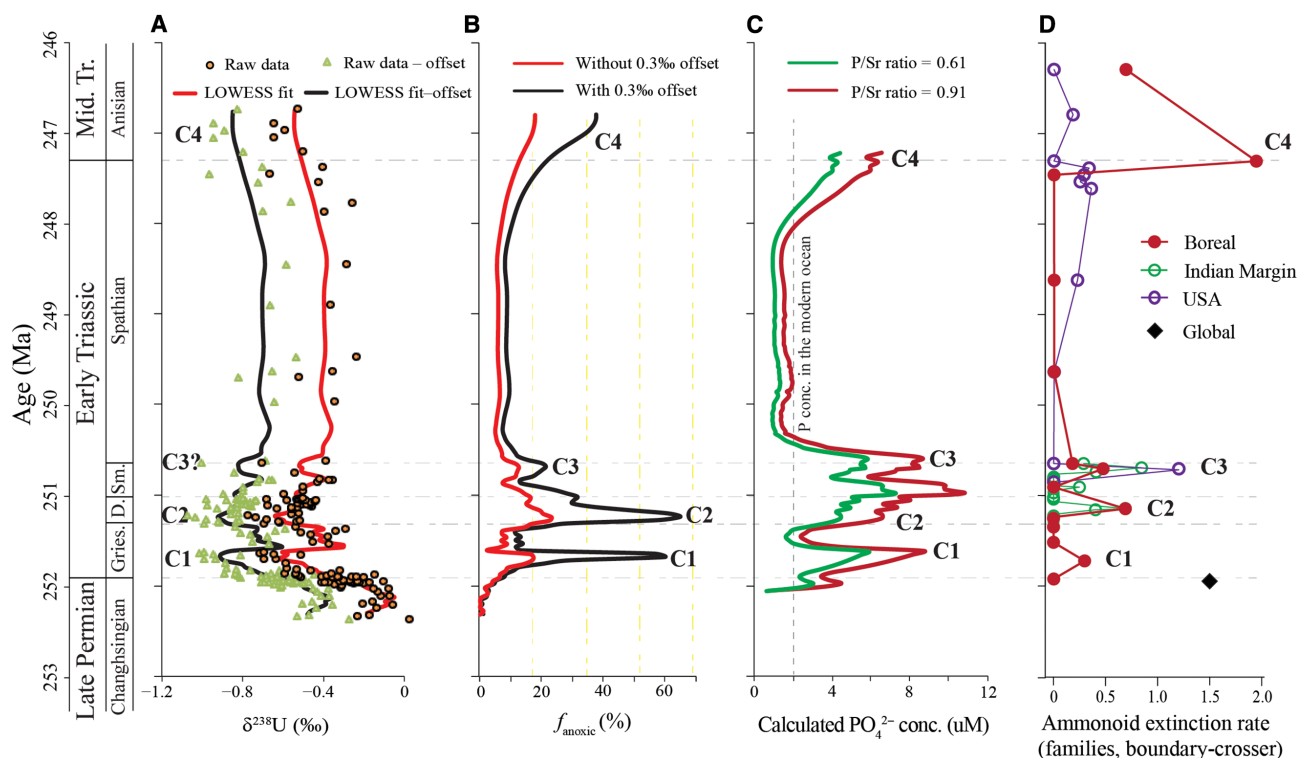


Fig. 3. Marine U-cycle mass balance model, calculated PO_4^{3-} concentrations, and ammonoid extinction rate curve. (A) $\delta^{238}\text{U}$ data with LOWESS smoothing fit; see the top of figure for legend. (B) Model estimates of anoxic seafloor area (f_{anoxic}) during Late Permian through Early/Middle Triassic time. The red and black lines denote modeling output without and with a diagenetic offset of 0.3‰, respectively. We note that the low $\delta^{238}\text{U}$ data resolution at the C3 event makes its model estimated timing and extent of oceanic anoxia with larger uncertainties compared to the other events. (C) Calculated PO_4^{3-} concentrations (conc.) in the Early Triassic ocean. The green and red lines denote modeling output assuming a P/Sr ratio of 0.61 and 0.91, respectively (see the Supplementary Materials). (D) Ammonoid extinction rate curve. See Fig. 2 for stage and substage abbreviations.

suggest 3 to 7×, 2 to 5×, 5 to 6×, and 1 to 2× increases in weathering fluxes across the C1, C2, C3, and C4 events, respectively (38, 39, 46). Intensified continental weathering would have flushed large amounts of PO_4^{3-} and other nutrients into the ocean, leading to higher marine productivity, higher organic carbon export from the euphotic zone, increased respiratory oxygen demand at depth, and a decrease in oceanic dissolved oxygen levels.

We propose that perturbations in marine redox chemistry were closely linked to changes in continental weathering fluxes and increased marine PO_4^{3-} levels. Phosphorus is commonly considered to be the ultimate biolimiting nutrient on marine productivity at geological time scales, and it plays a significant role in controlling the amount and spatial distribution of dissolved O_2 in the oceans (47–50). Increased phosphorus input to the ocean would have led to rapid (10^3 to 10^4 ka) increases in new production, higher O_2 demand, a larger vertical $\delta^{13}\text{C}$ gradient, and deep-water anoxia (48, 49, 51). We constructed a box model to estimate average seawater $[\text{PO}_4^{3-}]$ during the study interval (which is described in detail in the Supplementary Materials). We calculated riverine phosphorus inputs from $^{87}\text{Sr}/^{86}\text{Sr}$ -derived estimates of the continental weathering flux (38, 39), assuming a P/Sr ratio of 0.61 to 0.91 mol/mol (see the Supplementary Materials for justification of the P/Sr ratio). This ratio may have been locally amplified by preferential recycling of PO_4^{3-} through an anoxic and nonferruginous water column (50). Our calculations suggest that seawater PO_4^{3-} concentrations increased to $\sim 12\times [\text{PO}_4^{3-}]_0$, $\sim 10\times [\text{PO}_4^{3-}]_0$, $\sim 12\times [\text{PO}_4^{3-}]_0$, and $\sim 9\times [\text{PO}_4^{3-}]_0$ during the C1, C2, C3, and C4 events, where $[\text{PO}_4^{3-}]_0$ is the

initial PO_4^{3-} concentration in the pre-LPME Late Permian ocean (Fig. 3C). Sensitivity studies conducted using spatially resolved General Circulation Models (GCMs) of early Triassic climate and ocean circulation indicate that $[\text{PO}_4^{3-}]$ increases of this magnitude would have led to a significant expansion of anoxic water masses (47, 48). We therefore hypothesize that elevated seawater PO_4^{3-} levels associated with enhanced weathering fluxes played a key role in driving expansion of anoxia in the Early Triassic ocean.

In addition to enhanced nutrient inputs, intensified thermal stratification and reduced vertical mixing associated with rapid climatic warming may have further contributed to the expansion of oceanic anoxia (11). A previous study (14) argued that large $\delta^{13}\text{C}$ gradients in the Early Triassic ocean point to evidence of enhanced vertical stratification, yielding $\delta^{13}\text{C}$ gradients from the ocean surface to the mid-thermocline of ~ 8.5 , ~ 3.5 , ~ 7.8 , and ~ 2.2 ‰ during the C1 to C4 intervals, respectively, for sections from the northern Yangtze Platform and Nanpanjiang Basin in South China.

Relationship of oceanic anoxia and Early Triassic negative $\delta^{13}\text{C}$ excursions

The relationship between Early Triassic $\delta^{13}\text{C}$ excursions and marine redox changes has been the subject of lengthy debate (3, 14, 51–53). The negative $\delta^{13}\text{C}$ excursions have been linked to both higher marine productivity (51) and lower marine productivity (12, 14). In the present study, relationships among the $^{87}\text{Sr}/^{86}\text{Sr}$, $\delta^{238}\text{U}$, and $\delta^{13}\text{C}$ profiles support a relationship of negative $\delta^{13}\text{C}$ excursions to higher marine

productivity and expanded oceanic anoxia. However, this interpretation runs counter to the paradigmatic view of the marine carbon cycle, in which higher productivity and expanded anoxia increase the export flux of organic matter and thus stimulate a positive $\delta^{13}\text{C}$ excursion. A modeling study (52) suggested that the C1 to C4 negative $\delta^{13}\text{C}$ excursions might have been triggered by the injection of light carbon associated with eruption of the Siberian Traps or by methane release via contact metamorphism of West Siberian Coal Field deposits. Variations in the proportions of different carbon sources may account for differences in the shape and magnitude of Early Triassic carbon-isotope excursions (52), but determining secular variation in these influences [including volcanic carbon sources (52), marine productivity (51), and soil organic matter (53)] will require further study.

Relationship of oceanic anoxia to the PTB extinction and the protracted recovery of marine ecosystems

There is a growing body of evidence that the evolving redox structure of the oceans has been an important influence on the evolutionary trajectory of animals, including extinctions such as the LPME (22, 25, 54). Given their physiological requirements, oceanic anoxia can rapidly kill animals and potentially trigger restructuring of marine ecosystems. In the modern ocean, continental shelves comprise <7% of the seafloor area but host the majority of marine animal diversity, biomass, and organic carbon and phosphorus burial. A simple U-isotope mass balance model predicts that anoxic seafloor area expanded from an initial value of ~0.2% (assuming that precrisis redox conditions were similar to the modern ocean) to ~17 to 60%, ~23 to 65%, ~12 to 21%, and ~17 to 37% in the latest Changhsingian to earliest Griesbachian, the latest Griesbachian to earliest Dienerian, the mid-to-late Smithian, and the latest Spathian to earliest Anisian (that is, during C1 to C4), respectively (Fig. 3; see the Supplementary Materials for a description of box modeling of f_{anox}). Each expansion of anoxic waters likely covered a large proportion of continental shelves and upper slopes because numerous sections worldwide from such settings show evidence of anoxia (18–21, 55, 56).

The patterns of redox variation documented by the U-isotope record show a good first-order correspondence to ammonoid extinction rates during the Early Triassic (Fig. 3D; see the Supplementary Materials for a description of ammonoid extinction rates) (1, 5, 6). Intervals of expanded oceanic anoxia approximately coincided with extinction rate peaks in the end-Permian (251.94 Ma), possibly the mid-Griesbachian (251.7 Ma), the mid-Dienerian (251.2 Ma), the late Smithian (250.5 Ma), and the end-Spathian (247.2 Ma) (Fig. 3D). Ammonoid extinctions appear to be synchronous in multiple regions (for example, the Indian margin of the Neo-Tethys Ocean, the western Laurentian margin of the Panthalassic Ocean, and the Boreal ocean; Fig. 3D), suggesting that the crises were global in extent. Global diversity and extinction data for other invertebrate clades (for example, foraminifers, gastropods, bivalves, brachiopods, and ostracods) lack the high (biozone level) resolution of the ammonoid data but suffice to show that biodiversity levels were generally low until the early Middle Triassic, when a rapid recovery ensued (4, 8). Although benthic invertebrate communities may have undergone restructuring during the late Dienerian and late Smithian (57, 58), active swimming organisms such as ammonoids, as well as vertebrates (59), were more dramatically affected because of their active physiology and higher metabolic oxygen demand. Therefore, our results imply that the delayed Early Triassic marine recovery was a function of repeated environmental perturbations rather than the severity of the LPME event itself (18, 20).

Methods (extended description)

Fresh carbonate samples collected from the field were crushed into small fragments, cleaned using Milli-Q water, and dried. The freshest fragments without veins were hand-selected under a binocular microscope and powdered to ~200 mesh using an agate ball mill.

Approximately 3 g of each sample were dissolved in 1 M HCl using a 50-ml trace-metal-clean centrifuge tube and following this protocol: 6×5 ml of 1 M HCl was slowly added in the tube with a time gap of 10 min between steps. To continue the reaction, we added 1 ml of 10 M HCl every 25 min (producing 0.3 M HCl) for a total of five times. Finally, 1 M HCl was added to make a final volume of 45 ml. After sitting at room temperature for 24 hours, the samples were centrifuged to separate the supernatant and undissolved residues. This dissolution protocol uses a 1.5 \times excess of HCl to ensure complete dissolution of the carbonate, thus avoiding U-isotope fractionation from selective leaching of various carbonate phases.

Major, minor, and trace element concentrations were measured on a Thermo iCAP quadrupole inductively coupled plasma mass spectrometer (ICP-MS) at the W. M. Keck Laboratory for Environmental Biogeochemistry at ASU on splits from each supernatant. Typical precision was better than 3 and 5% for major and trace elements, respectively, based on repeated analysis of in-run check standards.

Before U-isotope column chemistry (ion exchange chromatography), appropriate amounts of the IRMM 3636 ^{236}U : ^{233}U double spike (22, 24, 27) were added to an amount of sample solution corresponding to 400 to 500 ng of U to facilitate correction for instrumental mass fractionation and any U-isotope fractionation during column chemistry. The spike-sample mixtures were evaporated to dryness and taken up in 3 M HNO_3 . Uranium for isotopic analysis was purified using the Uranium and TEtraValents Actinides (UTEVA) method (22, 24, 27). Following column chemistry, samples were evaporated in a mixture of concentrated nitric acid and 32% hydrogen peroxide repeatedly (3 \times) to oxidize any organic materials leached from the Eichrom UTEVA resin. All samples have been put through U-isotope column chemistry twice to completely remove matrix ions. Purified U was dissolved in 0.32 M HNO_3 and diluted to a U concentration of 50 parts per billion (ppb). Uranium isotopes were measured at ASU on a ThermoFinnigan Neptune multicollector ICP-MS at low mass resolution. When using a nebulizer (100 $\mu\text{l}/\text{min}$), a 50-ppb sample solution yielded 30 to 40 V of ^{238}U signal on a 10^{11} -ohm amplifier. The standard solution CRM145 (50 ppb of U) was analyzed every two samples. Two secondary standards (CRM129a and an in-house Ricca ICP solution) were measured after every 15 sample measurements. Sample $\delta^{238}\text{U}$ values were normalized by the average of the bracketing CRM145 standards. CRM145 shares its isotopic composition with another common standard CRM112a, from which it was prepared (24, 27, 29). The measured isotopic compositions of standards CRM145, CRM129a, and Ricca are $-0.00 \pm 0.07\text{‰}$ (2σ , $n = 61$), $-1.74 \pm 0.06\text{‰}$ (2σ , $n = 9$), and $-0.28 \pm 0.08\text{‰}$ (2σ , $n = 7$), respectively.

SUPPLEMENTARY MATERIALS

Supplementary material for this article is available at <http://advances.sciencemag.org/cgi/content/full/4/4/e1602921/DC1>

The study section

Evidence for primary seawater $\delta^{238}\text{U}$ values

Compilation of global carbonate $\delta^{238}\text{U}$ records for PTB interval

Possible timing of onset of oceanic anoxia

Age-thickness model for Zai section

Cross-correlation analysis

High-resolution intercomparison of $\delta^{13}\text{C}$, $^{87}\text{Sr}/^{86}\text{Sr}$, and $\delta^{238}\text{U}$ recordsEstimation of weathering rates and seawater PO_4^{3-} levels in the Early Triassic oceanBox model estimates for f_{anox}

Patterns of marine invertebrate clade recovery following the LPME

Ammonoid extinction rates

table S1. Strontium and phosphorus model parameterization.

table S2. Uranium box model parameterization.

fig. S1. Geochemical profile of Zal, Iran.

fig. S2. Diagenetic evaluation cross-plots of $\delta^{238}\text{U}$ -[Sr], $\delta^{238}\text{U}$ -Mn/Sr, and $\delta^{238}\text{U}$ -Mg/Ca

(mol/mol) of all samples, samples below 3.5 m, samples between 3.5 and 500 m, and samples above 500 m.

fig. S3. Cross-plots of $\delta^{238}\text{U}$ -Rb/Sr and $\delta^{238}\text{U}$ -U/Al ratio [parts per million/weight % (wt %)] for all samples and samples below and above 500 m.fig. S4. Cross-plots of $\delta^{238}\text{U}$ -Mn/Sr, $\delta^{238}\text{U}$ -Mg/Ca, $\delta^{238}\text{U}$ -Rb/Sr, and $\delta^{238}\text{U}$ -U/Al (wt %) for anoxic events 1 and 2.fig. S5. Cross-plots of $\delta^{238}\text{U}$ -Mn/Sr, $\delta^{238}\text{U}$ -Mg/Ca, $\delta^{238}\text{U}$ -Rb/Sr, and $\delta^{238}\text{U}$ -U/Al (wt %) for anoxic events 3 and 4.fig. S6. Cross-plots of $\delta^{13}\text{C}$ - $\delta^{18}\text{O}$ for the Zal section.fig. S7. Location of Iran, South China, and Turkey during the Permian-Triassic transition, ~252 Ma (modified after Payne *et al.* (60)).

fig. S8. Comparison of U- and C-isotope profiles for Zal, Dawen, Dajiang, Taşkent, and Kamura.

fig. S9. A LOWESS trend showing inferred timing of onset of latest Permian oceanic anoxia.

fig. S10. Age-depth model for the Zal, Iran study section.

fig. S11. Cross-correlation analysis of LOWESS-smoothed curves for U-C-Sr isotope records.

fig. S12. $^{87}\text{Sr}/^{86}\text{Sr}$ -derived estimates of the continental weathering flux and the calculated seawater PO_4^{3-} concentrations for the Early Triassic ocean.

fig. S13. Interregional ammonoid zonation scheme.

dataset S1. $\delta^{238}\text{U}$ data with associated geochemical data.

References (61–115)

REFERENCES AND NOTES

- Z.-Q. Chen, M. J. Benton, The timing and pattern of biotic recovery following the end-Permian mass extinction. *Nat. Geosci.* **5**, 375–383 (2012).
- S. D. Burgess, S. Bowring, S.-z. Shen, High-precision timeline for Earth's most severe extinction. *Proc. Natl. Acad. Sci. U.S.A.* **111**, 3316–3321 (2014).
- J. L. Payne, D. J. Lehrmann, J. Wei, M. J. Orchard, D. P. Schrag, A. H. Knoll, Large perturbations of the carbon cycle during recovery from the end-permian extinction. *Science* **305**, 506–509 (2004).
- H. Wei, J. Shen, S. D. Schoepfer, L. Krystyn, S. Richo, T. J. Algeo, Environmental controls on marine ecosystem recovery following mass extinctions, with an example from the Early Triassic. *Earth Sci. Rev.* **149**, 108–135 (2015).
- A. Brayard, G. Escarguel, H. Bucher, C. Monnet, T. Brühwiler, N. Goudemand, T. Galfetti, J. Guex, Good genes and good luck: Ammonoid diversity and the end-Permian mass extinction. *Science* **325**, 1118–1121 (2009).
- S. M. Stanley, Evidence from ammonoids and conodonts for multiple Early Triassic mass extinctions. *Proc. Natl. Acad. Sci. U.S.A.* **106**, 15264–15267 (2009).
- Z.-Q. Chen, J. Tong, M. L. Fraiser, Trace fossil evidence for restoration of marine ecosystems following the end-Permian mass extinction in the Lower Yangtze region, South China. *Palaeogeogr. Palaeoclimatol. Palaeoecol.* **299**, 449–474 (2011).
- J. L. Payne, M. Summers, B. L. Rego, D. Altiner, J. Wei, M. Yu, D. J. Lehrmann, Early and Middle Triassic trends in diversity, evenness, and size of foraminifers on a carbonate platform in south China: Implications for tempo and mode of biotic recovery from the end-Permian mass extinction. *Paleobiology* **37**, 409–425 (2011).
- H. J. Song, P. B. Wignall, Z.-Q. Chen, J. Tong, D. P. G. Bond, X. Lai, X. Zhao, H. Jiang, C. Yan, Z. Niu, J. Chen, H. Yang, Y. Wang, Recovery tempo and pattern of marine ecosystems after the end-Permian mass extinction. *Geology* **39**, 739–742 (2011).
- R. V. Solé, J. M. Montoya, D. H. Erwin, Recovery after mass extinction: Evolutionary assembly in large-scale biosphere dynamics. *Philos. Trans. R. Soc. Lond. B Biol. Sci.* **357**, 697–707 (2002).
- Y. Sun, M. M. Joachimski, P. B. Wignall, C. Yan, Y. Chen, H. Jiang, L. Wang, X. Lai, Lethally hot temperatures during the Early Triassic greenhouse. *Science* **338**, 366–370 (2012).
- S. E. Grasby, B. Beauchamp, J. Knies, Early Triassic productivity crises delayed recovery from world's worst mass extinction. *Geology* **44**, 779–782 (2016).
- G. J. Retallack, N. D. Sheldon, P. F. Carr, M. Fanning, C. A. Thompson, M. L. Williams, B. G. Jones, Multiple Early Triassic greenhouse crises impeded recovery from Late Permian mass extinction. *Palaeogeogr. Palaeoclimatol. Palaeoecol.* **308**, 233–251 (2011).
- H. Song, J. Tong, T. J. Algeo, M. Horacek, H. Qiu, H. Song, L. Tian, Z.-Q. Chen, Large vertical $\delta^{13}\text{C}_{\text{DIC}}$ gradients in Early Triassic seas of the South China craton: Implications for oceanographic changes related to Siberian Traps volcanism. *Glob. Planet. Change* **105**, 7–20 (2013).
- M. Horacek, S. Richo, R. Brandner, L. Krystyn, C. Spötl, Evidence for recurrent changes in Lower Triassic oceanic circulation of the Tethys: The $\delta^{13}\text{C}$ record from marine sections in Iran. *Palaeogeogr. Palaeoclimatol. Palaeoecol.* **252**, 355–369 (2007).
- G. Zhang, X. Zhang, D. Hu, D. Li, T. J. Algeo, J. Farquhar, C. M. Henderson, L. Qin, M. Shen, D. Shen, S. D. Schoepfer, K. Chen, Y. Shen, Redox chemistry changes in the Panthalassic Ocean linked to the end-Permian mass extinction and delayed Early Triassic biotic recovery. *Proc. Natl. Acad. Sci. U.S.A.* **114**, 1806–1810 (2017).
- Y. Isozaki, Permo-Triassic boundary superanoxia and stratified superocean: Records from lost deep sea. *Science* **276**, 235–238 (1997).
- K. V. Lau, K. Maher, D. Altiner, B. M. Kelley, L. R. Kump, D. J. Lehrmann, J. C. Silva-Tamayo, K. L. Weaver, M. Yu, J. L. Payne, Marine anoxia and delayed Earth system recovery after the end-Permian extinction. *Proc. Natl. Acad. Sci. U.S.A.* **113**, 2360–2365 (2016).
- H. Song, P. B. Wignall, J. Tong, D. P. G. Bond, H. Song, X. Lai, K. Zhang, H. Wang, Y. Chen, Geochemical evidence from bio-apatite for multiple oceanic anoxic events during Permian-Triassic transition and the link with end-Permian extinction and recovery. *Earth Planet. Sci. Lett.* **353–354**, 12–21 (2012).
- S. E. Grasby, B. Beauchamp, A. Embry, H. Sanei, Recurrent Early Triassic ocean anoxia. *Geology* **41**, 175–178 (2013).
- M. O. Clarkson, R. A. Wood, S. W. Poulton, S. Richo, R. J. Newton, S. A. Kasemann, F. Bowyer, L. Krystyn, Dynamic anoxic ferruginous conditions during the end-Permian mass extinction and recovery. *Nat. Commun.* **7**, 12236 (2016).
- G. A. Brenneke, A. D. Herrmann, T. J. Algeo, A. D. Anbar, Rapid expansion of oceanic anoxia immediately before the end-Permian mass extinction. *Proc. Natl. Acad. Sci. U.S.A.* **108**, 17631–17634 (2011).
- M. Elrick, V. Polyak, T. J. Algeo, S. Romaniello, Y. Asmerom, A. D. Herrmann, A. D. Anbar, L. Zhao, Z.-Q. Chen, Global-ocean redox variation during the middle-late Permian through Early Triassic based on uranium isotope and Th/U trends of marine carbonates. *Geology* **45**, 163–166 (2017).
- S. J. Romaniello, A. D. Herrmann, A. D. Anbar, Uranium concentrations and $^{238}\text{U}/^{235}\text{U}$ isotope ratios in modern carbonates from the Bahamas: Assessing a novel paleoredox proxy. *Chem. Geol.* **362**, 305–316 (2013).
- F. Zhang, T. J. Algeo, S. J. Romaniello, Y. Cui, L. Zhao, Z.-Q. Chen, A. D. Anbar, Congruent Permian-Triassic $\delta^{238}\text{U}$ records at Panthalassic and Tethyan sites: Confirmation of global-oceanic anoxia and validation of the U-isotope paleoredox proxy. *Geology*, in press (2018).
- T.-L. Ku, K. G. Knauss, G. G. Mathieu, Uranium in open ocean: Concentration and isotopic composition. *Deep Sea Res.* **24**, 1005–1017 (1977).
- S. Weyer, A. D. Anbar, A. Gerdes, G. W. Gordon, T. J. Algeo, E. A. Boyle, Natural fractionation of $^{238}\text{U}/^{235}\text{U}$. *Geochim. Cosmochim. Acta* **72**, 345–359 (2008).
- C. H. Stirling, M. B. Andersen, E.-K. Potter, A. N. Halliday, Low-temperature isotopic fractionation of uranium. *Earth Planet. Sci. Lett.* **264**, 208–225 (2007).
- F. L. H. Tissot, N. Dauphas, Uranium isotopic compositions of the crust and ocean: Age corrections, U budget and global extent of modern anoxia. *Geochim. Cosmochim. Acta* **167**, 113–143 (2015).
- M. B. Andersen, C. H. Stirling, S. Weyer, Uranium isotope fractionation. *Rev. Mineral. Geochem.* **82**, 799–850 (2017).
- J. L. Morford, S. Emerson, The geochemistry of redox sensitive trace metals in sediments. *Geochim. Cosmochim. Acta* **63**, 1735–1750 (1999).
- C. Holmden, M. Amini, R. Francois, Uranium isotope fractionation in Saanich Inlet: A modern analog study of a paleoredox tracer. *Geochim. Cosmochim. Acta* **153**, 202–215 (2015).
- J. M. Rolison, C. H. Stirling, R. Middag, M. J. A. Rijkenberg, Uranium stable isotope fractionation in the Black Sea: Modern calibration of the $^{238}\text{U}/^{235}\text{U}$ paleo-redox proxy. *Geochim. Cosmochim. Acta* **203**, 69–88 (2017).
- J. Noordmann, S. Weyer, C. Montoya-Pino, O. Dellwig, N. Neubert, S. Eckert, M. Paetzel, M. E. Böttcher, Uranium and molybdenum isotope systematics in modern euxinic basins: Case studies from the central Baltic Sea and the Kyllaren fjord (Norway). *Chem. Geol.* **396**, 182–195 (2015).
- K. V. Lau, F. A. Macdonald, K. Maher, J. L. Payne, Uranium isotope evidence for temporary ocean oxygenation in the aftermath of the Sturtian Snowball Earth. *Earth Planet. Sci. Lett.* **458**, 282–292 (2017).
- X. Chen, S. J. Romaniello, A. D. Herrmann, L. E. Wasylenki, A. D. Anbar, Uranium isotope fractionation during coprecipitation with aragonite and calcite. *Geochim. Cosmochim. Acta* **188**, 189–207 (2016).
- S. Richo, L. Krystyn, A. Baud, Rainer Brandner, Micha Horacek, Parvin Mohtat-Aghai, Permian-Triassic boundary interval in the Middle East (Iran and N. Oman): Progressive environmental change from detailed carbonate carbon isotope marine curve and sedimentary evolution. *J. Asian Earth Sci.* **39**, 236–253 (2010).
- A. R. C. Sedlacek, M. R. Saltzman, T. J. Algeo, M. Horacek, R. Brandner, K. Foland, R. F. Denniston, $^{87}\text{Sr}/^{86}\text{Sr}$ stratigraphy from the Early Triassic of Zal, Iran: Linking

- temperature to weathering rates and the tempo of ecosystem recovery. *Geology* **42**, 779–782 (2014).
39. H. Song, P. B. Wignall, J. Tong, H. Song, J. Chen, D. Chu, L. Tian, M. Luo, K. Zong, Y. Chen, X. Lai, K. Zhang, H. Wang, Integrated Sr isotope variations and global environmental changes through the Late Permian to early Late Triassic. *Earth Planet. Sci. Lett.* **424**, 140–147 (2015).
 40. A. J. Kaufman, A. H. Knoll, Neoproterozoic variations in the C-isotopic composition of seawater: Stratigraphic and biogeochemical implications. *Precambrian Res.* **73**, 27–49 (1995).
 41. G. M. Henderson, N. C. Slowey, G. A. Haddad, Fluid flow through carbonate platforms: Constraints from $^{234}\text{U}/^{238}\text{U}$ and Cl^- in Bahamas pore-waters. *Earth Planet. Sci. Lett.* **169**, 99–111 (1999).
 42. J. Shen, T. J. Algeo, Q. Hu, N. Zhang, L. Zhou, W. Xia, S. Xie, Q. Feng, Negative C-isotope excursions at the Permian-Triassic boundary linked to volcanism. *Geology* **40**, 963–966 (2012).
 43. S. D. Burgess, S. A. Bowring, High-precision geochronology confirms voluminous magmatism before, during, and after Earth's most severe extinction. *Sci. Adv.* **1**, e1500470 (2015).
 44. P. A. Martin, D. W. Lea, T. A. Mashiotta, T. Papenfuss, M. Sarnthein, Variation of foraminiferal Sr/Ca over Quaternary glacial-interglacial cycles: Evidence for changes in mean ocean Sr/Ca? *Geochem. Geophys. Geosyst.* **1**, 1004 (2000).
 45. T. Tütken, A. Eisenhauer, B. Wiegand, B. T. Hansen, Glacial-interglacial cycles in Sr and Nd isotopic composition of Arctic marine sediments triggered by the Svalbard/Barents Sea ice sheet. *Mar. Geol.* **182**, 351–372 (2002).
 46. T. J. Algeo, R. J. Twitchett, Anomalous Early Triassic sediment fluxes due to elevated weathering rates and their biological consequences. *Geology* **38**, 1023–1026 (2010).
 47. C. Winguth, A. M. E. Winguth, Simulating Permian-Triassic oceanic anoxia distribution: Implications for species extinction and recovery. *Geology* **40**, 127–130 (2012).
 48. K. M. Meyer, A. Ridgwell, J. L. Payne, The influence of the biological pump on ocean chemistry: Implications for long-term trends in marine redox chemistry, the global carbon cycle, and marine animal ecosystems. *Geobiology* **14**, 207–219 (2016).
 49. T. M. Lenton, R. A. Boyle, S. W. Poulton, G. A. Shields-Zhou, N. J. Butterfield, Co-evolution of eukaryotes and ocean oxygenation in the Neoproterozoic era. *Nat. Geosci.* **7**, 257–265 (2014).
 50. P. Van Cappellen, E. D. Ingall, Benthic phosphorus regeneration, net primary production, and ocean anoxia: A model of the coupled marine biogeochemical cycles of carbon and phosphorus. *Paleoceanography* **9**, 677–692 (1994).
 51. K. M. Meyer, M. Yu, A. B. Jost, B. M. Kelley, J. L. Payne, $\delta^{13}\text{C}$ evidence that high primary productivity delayed recovery from end-Permian mass extinction. *Earth Planet. Sci. Lett.* **302**, 378–384 (2011).
 52. J. L. Payne, L. R. Kump, Evidence for recurrent Early Triassic massive volcanism from quantitative interpretation of carbon isotope fluctuations. *Earth Planet. Sci. Lett.* **256**, 264–277 (2007).
 53. M. A. Sephton, C. V. Looy, H. Brinkhuis, P. B. Wignall, J. W. de Leeuw, H. Visscher, Catastrophic soil erosion during the end-Permian biotic crisis. *Geology* **33**, 941–944 (2005).
 54. Q. Feng, T. J. Algeo, Evolution of oceanic redox conditions during the Permian-Triassic transition: Evidence from deepwater radiolarian facies. *Earth Sci. Rev.* **137**, 34–51 (2014).
 55. D. P. G. Bond, P. B. Wignall, Pyrite framboid study of marine Permian-Triassic boundary sections: A complex anoxic event and its relationship to contemporaneous mass extinction. *Geol. Soc. Am. Bull.* **122**, 1265–1279 (2010).
 56. K. Grice, C. Cao, G. D. Love, M. E. Böttcher, R. J. Twitchett, E. Grosjean, R. E. Summons, S. C. Turgeon, W. Dunning, Y. Jin, Photic zone euxinia during the Permian-Triassic superanoxic event. *Science* **307**, 706–709 (2005).
 57. R. Hofmann, M. Hautmann, A. Brayard, A. Nützel, K. G. Bylund, J. F. Jenks, E. Vennin, N. Olivier, H. Bucher, Recovery of benthic marine communities from the end-Permian mass extinction at the low latitudes of eastern Panthalassa. *Palaeontology* **57**, 547–589 (2014).
 58. W. J. Foster, S. Danise, G. D. Price, R. J. Twitchett, Subsequent biotic crises delayed marine recovery following the late Permian mass extinction event in northern Italy. *PLOS ONE* **12**, e0172321 (2017).
 59. T. M. Scheyer, C. Romano, J. Jenks, H. Bucher, Early Triassic marine biotic recovery: The predators' perspective. *PLOS ONE* **9**, e88987 (2014).
 60. J. L. Payne, D. J. Lehmann, D. Follett, M. Seibel, L. R. Kump, A. Riccardi, D. Altiner, H. Sano, J. Wei, Erosional truncation of uppermost Permian shallow-marine carbonates and implications for Permian-Triassic boundary events. *Geol. Soc. Am. Bull.* **119**, 771–784 (2007).
 61. L. Leda, D. Korn, A. Ghaderi, V. Hairapetian, U. Struck, W. U. Reimold, Lithostratigraphy and carbonate microfacies across the Permian-Triassic boundary near Julfa (NW Iran) and in the Baghuk Mountains (Central Iran). *Facies* **60**, 295–325 (2014).
 62. J. L. Banner, G. N. Hanson, Calculation of simultaneous isotopic and trace element variations during water-rock interaction with applications to carbonate diagenesis. *Geochim. Cosmochim. Acta* **54**, 3123–3137 (1990).
 63. J. Veizer, Chemical diagenesis of carbonates: Theory and application of trace element technique, in *Stable Isotopes in Sedimentary Geology (SEPM Society for Sedimentary Geology, 1983)*, vol. 10, Society of Economic Paleontologists and Mineralogists Short Course Notes, pp. III-1–III-100.
 64. V. C. Vahrenkamp, P. K. Swart, New distribution coefficient for the incorporation of strontium into dolomite and its implications for the formation of ancient dolomites. *Geology* **18**, 387–391 (1990).
 65. S. J. Mazzullo, Geochemical and neomorphic alteration of dolomite: A review. *Carbonate. Evaporite* **7**, 21–37 (1992).
 66. J. D. Rimstidt, A. Balog, J. Webb, Distribution of trace elements between carbonate minerals and aqueous solutions. *Geochim. Cosmochim. Acta* **62**, 1851–1863 (1998).
 67. R. L. Rudnick, S. Gao, Major elements of Earth Crust, in *Treatise on Geochemistry*, H. D. Holland, K. K. Turekian, Eds. (Elsevier, 2003), vol. 3, pp. 1–64.
 68. T. Algeo, C. M. Henderson, B. Ellwood, H. Rowe, E. Elswick, S. Bates, T. Lyons, J. C. Hower, C. Smith, B. Maynard, L. E. Hays, R. E. Summons, J. Fulton, K. H. Freeman, Evidence for a diachronous Late Permian marine crisis from the Canadian Arctic region. *Geol. Soc. Am. Bull.* **124**, 1424–1448 (2012).
 69. T. J. Algeo, C. M. Henderson, J. Tong, Q. Feng, H. Yin, R. V. Tyson, Plankton and productivity during the Permian-Triassic boundary crisis: An analysis of organic carbon fluxes. *Glob. Planet. Change* **105**, 52–67 (2013).
 70. D. J. Lehmann, J. Ramezani, S. A. Bowring, M. W. Martin, P. Montgomery, P. Enos, J. L. Payne, M. J. Orchard, W. Hongmei, W. Jiayong, Timing of recovery from the end-Permian extinction: Geochronologic and biostratigraphic constraints from south China. *Geology* **34**, 1053–1056 (2006).
 71. M. Ovtcharova, H. Bucher, U. Schaltegger, T. Galfetti, A. Brayard, J. Guex, New Early to Middle Triassic U-Pb ages from South China: Calibration with ammonoid biochronozones and implications for the timing of the Triassic biotic recovery. *Earth Planet. Sci. Lett.* **243**, 463–475 (2006).
 72. T. Galfetti, H. Bucher, M. Ovtcharova, U. Schaltegger, A. Brayard, T. Brühwiler, N. Goudemand, H. Weissert, P. A. Hochuli, F. Cordey, K. Guodun, Timing of the Early Triassic carbon cycle perturbations inferred from new U-Pb ages and ammonoid biochronozones. *Earth Planet. Sci. Lett.* **258**, 593–604 (2007).
 73. G. Guo, J. Tong, S. Zhang, J. Zhang, L. Bai, Cyclostratigraphy of the Induan (Early Triassic) in West Pingdingshan Section, Chaohu, Anhui Province. *Sci. China Ser. D* **51**, 22–29 (2008).
 74. J. C. Davis, R. J. Sampson, *Statistics and Data Analysis in Geology* (Wiley, 1986).
 75. R. M. Dunk, R. A. Mills, W. J. Jenkins, A reevaluation of the oceanic uranium budget for the Holocene. *Chem. Geol.* **190**, 45–67 (2002).
 76. R. E. Zeebe, D. Wolf-Gladrow, *CO₂ in Seawater: Equilibrium, Kinetics, Isotopes* (Elsevier, 2001), Series in Oceanography, vol. 65, 360 pp.
 77. T. J. Algeo, K. Kuwahara, H. Sano, S. Bates, T. Lyons, E. Elswick, L. Hinnov, B. Ellwood, J. Moser, J. B. Maynard, Spatial variation in sediment fluxes, redox conditions, and productivity in the Permian-Triassic Panthalassic Ocean. *Palaeogeogr. Palaeoclimatol. Palaeoecol.* **308**, 65–83 (2011).
 78. H. Y. Song, J. Tong, T. J. Algeo, H. Song, H. Qiu, Y. Zhu, L. Tian, S. Bates, T. W. Lyons, G. Luo, L. R. Kump, Early Triassic seawater sulfate drawdown. *Geochim. Cosmochim. Acta* **128**, 95–113 (2014).
 79. F. M. Richter, K. K. Turekian, Simple models for the geochemical response of the ocean to climatic and tectonic forcing. *Earth Planet. Sci. Lett.* **119**, 121–131 (1993).
 80. Y. Goddérès, L. M. François, The Cenozoic evolution of the strontium and carbon cycles: Relative importance of continental erosion and mantle exchanges. *Chem. Geol.* **126**, 169–190 (1995).
 81. M. F. Schaller, J. D. Wright, D. V. Kent, Atmospheric Pco_2 perturbations associated with the Central Atlantic Magmatic Province. *Science* **331**, 1404–1409 (2011).
 82. F. Horton, Did phosphorus derived from the weathering of large igneous provinces fertilize the Neoproterozoic ocean? *Geochem. Geophys. Geosyst.* **16**, 1723–1738 (2015).
 83. M. R. Palmer, J. M. Edmond, The strontium isotope budget of the modern ocean. *Earth Planet. Sci. Lett.* **92**, 11–26 (1989).
 84. A. Paytan, K. McLaughlin, The oceanic phosphorus cycle. *Chem. Rev.* **107**, 563–576 (2007).
 85. G. N. Baturin, Phosphorus cycle in the ocean. *Lithol. Miner. Resour.* **38**, 101–119 (2003).
 86. P. Van Cappellen, E. D. Ingall, Redox stabilization of the atmosphere and oceans by phosphorus-limited marine productivity. *Science* **271**, 493–496 (1996).
 87. C. T. Reinhard, N. J. Planavsky, B. C. Gill, K. Ozaki, L. J. Robbins, T. W. Lyons, W. W. Fischer, C. Wang, D. B. Cole, K. O. Konhauser, Evolution of the global phosphorus cycle. *Nature* **541**, 386–389 (2017).
 88. T. Tyrrell, The relative influences of nitrogen and phosphorus on oceanic primary production. *Nature* **400**, 525–531 (1999).
 89. P. N. Froelich, Kinetic control of dissolved phosphate in natural rivers and estuaries: A primer on the phosphate buffer mechanism. *Limnol. Oceanogr.* **33**, 649–668 (1988).
 90. E. Ingall, R. Jahnke, Influence of water-column anoxia on the elemental fractionation of carbon and phosphorus during sediment diagenesis. *Mar. Geol.* **139**, 219–229 (1997).

91. I. C. Handoh, T. M. Lenton, Periodic mid-Cretaceous oceanic anoxic events linked by oscillations of the phosphorus and oxygen biogeochemical cycles. *Global Biogeochem. Cycles* **17**, 1092 (2003).
92. H. P. Mort, T. Adatte, K. B. Föllmi, G. Keller, P. Steinmann, V. Matera, Z. Berner, D. Stüben, Phosphorus and the roles of productivity and nutrient recycling during oceanic anoxic event 2. *Geology* **35**, 483–486 (2007).
93. F. Albarède, A. Michard, J. F. Minster, G. Michard, $^{87}\text{Sr}/^{86}\text{Sr}$ ratios in hydrothermal waters and deposits from the East Pacific Rise at 21°N. *Earth Planet. Sci. Lett.* **55**, 229–236 (1981).
94. F. M. Richter, Y. Liang, The rate and consequences of Sr diagenesis in deep-sea carbonates. *Earth Planet. Sci. Lett.* **117**, 553–565 (1993).
95. D. A. Hodell, G. A. Mead, P. A. Mueller, Variation in the strontium isotopic composition of seawater (8 Ma to present): Implications for chemical weathering rates and dissolved fluxes to the oceans. *Chem. Geol.* **80**, 291–307 (1990).
96. M. B. Andersen, S. Romaniello, D. Vance, S. H. Little, R. Herdman, T. W. Lyons, A modern framework for the interpretation of $^{238}\text{U}/^{235}\text{U}$ in studies of ancient ocean redox. *Earth Planet. Sci. Lett.* **400**, 184–194 (2014).
97. C. Montoya-Pino, S. Weyer, A. D. Anbar, J. Pross, W. Oschmann, B. van de Schootbrugge, H. W. Arz, Global enhancement of ocean anoxia during Oceanic Anoxic Event 2: A quantitative approach using U isotopes. *Geology* **38**, 315–318 (2010).
98. X. Wang, N. J. Planavsky, C. T. Reinhard, J. R. Hein, T. M. Johnson, A Cenozoic seawater redox record derived from $^{238}\text{U}/^{235}\text{U}$ in ferromanganese crusts. *Am. J. Sci.* **316**, 64–83 (2016).
99. M. J. Orchard, Conodont diversity and evolution through the latest Permian and Early Triassic upheavals. *Palaeogeogr. Palaeoclimatol. Palaeoecol.* **252**, 93–117 (2007).
100. M. L. Fraiser, D. J. Bottjer, The non-actualistic early Triassic gastropod fauna: A case study of the lower triassic sinbad limestone member. *Palaios* **19**, 259–275 (2004).
101. J. L. Payne, Evolutionary dynamics of gastropod size across the end-Permian extinction and through the Triassic recovery interval. *Paleobiology* **31**, 269–290 (2005).
102. R. J. Twitchett, The Lilliput effect in the aftermath of the end-Permian extinction event. *Palaeogeogr. Palaeoclimatol. Palaeoecol.* **252**, 132–144 (2007).
103. S. B. Pruss, D. J. Bottjer, Early Triassic trace fossils of the western United States and their implications for prolonged environmental stress from the end-permian mass extinction. *Palaios* **19**, 551–564 (2004).
104. J. L. Payne, D. J. Lehrmann, J. Wei, A. H. Knoll, The pattern and timing of biotic recovery from the end-Permian extinction on the great bank of guizhou, guizhou province, china. *Palaios* **21**, 63–85 (2006).
105. D. Ware, H. Bucher, A. Brayard, E. Schneebeli-Hermann, T. Brühwiler, High-resolution biochronology and diversity dynamics of the Early Triassic ammonoid recovery: The Dienerian faunas of the Northern Indian Margin. *Palaeogeogr. Palaeoclimatol. Palaeoecol.* **440**, 363–373 (2015).
106. J. Alroy, Accurate and precise estimates of origination and extinction rates. *Paleobiology* **40**, 374–397 (2014).
107. A. Brayard, K. G. Bylund, J. F. Jenks, D. A. Stephen, N. Olivier, G. Escarguel, E. Fara, E. Vennin, Smithian ammonoid faunas from Utah: Implications for Early Triassic biostratigraphy, correlation and basinal paleogeography. *Swiss J. Palaeontol.* **132**, 141–219 (2013).
108. E. T. Tozer, Canadian Triassic ammonoid faunas. *Geol. Surv. Canada Bull.* **467**, 1–663 (1994).
109. S. P. Ermakova, *Zonal'nyi Standart Boreal'nogo Nizhnego Trias* (Nauka, 2002).
110. Y. D. Zakharov, N. Mousavi Abnavi, The ammonoid recovery after the end-Permian mass extinction: Evidence from the Iran-Transcaucasia area, Siberia, Primorye, and Kazakhstan. *Acta Palaeontol. Pol.* **58**, 127–147 (2013).
111. T. Brühwiler, H. Bucher, A. Brayard, N. Goudemand, High-resolution biochronology and diversity dynamics of the Early Triassic ammonoid recovery: The Smithian faunas of the Northern Indian Margin. *Palaeogeogr. Palaeoclimatol. Palaeoecol.* **297**, 491–501 (2010).
112. J. Guex, A. Hungerbühler, J. F. Jenks, L. O'Dogherty, V. Atudorei, D. G. Taylor, H. Bucher, A. Bartolini, Spathian (Lower Triassic) ammonoids from western USA (Idaho, California, Utah and Nevada), in *Mémoires de Géologie (Lausanne)*, (Université de Lausanne, 2010), vol. 49, pp. 1–82.
113. H. Bucher, Lower Anisian ammonoids from the northern Humboldt Range (northwestern Nevada, USA) and their bearing upon the Lower-Middle Triassic boundary. *Ecolgae Geol. Helv.* **82**, 945–1002 (1989).
114. J. Chen, T. W. Beatty, C. M. Henderson, H. Rowe, Conodont biostratigraphy across the Permian–Triassic boundary at the Dawen section, Great Bank of Guizhou, Guizhou Province, South China: Implications for the Late Permian extinction and correlation with Meishan. *J. Asian Earth Sci.* **36**, 442–458 (2009).
115. L. Zhang, M. J. Orchard, T. J. Algeo, Z.-Q. Chen, Z. Lyu, L. Zhao, K. Kaiho, B. Ma, S. Liu, An intercalibrated Triassic conodont succession and carbonate carbon isotope profile, Kamura, Japan. *Palaeogeogr. Palaeoclimatol. Palaeoecol.*, in press (2017).

Acknowledgments: We thank A. Baud, L. Krystyn, R. Brandner, M. Tayebah Mohtat, and B. Hamdi for help in the field and G. Gordon for her assistance with the laboratory work. We also thank Dr. Noah Planavsky and the two anonymous reviewers for their constrictive comments on our manuscript. We also thank Dr. Noah Planavsky and the two anonymous reviewers for their constructive comments on our manuscript. **Funding:** This research is supported by funding from the NASA Exobiology Program (award NNX13AJ71G) and the NSF Frontiers in Earth System Dynamics program (award EAR-1338810). **Author contributions:** F.Z., S.J.R., T.J.A., and A.D.A. designed research. F.Z. performed research and analyzed data. S.R. and M.H. undertook fieldwork and provided sedimentological framework. F.Z., S.J.R., and K.V.L. contributed to the model calculations. All authors contributed with discussions. F.Z. prepared the manuscript with significant inputs from S.J.R., T.J.A., and A.D.A. **Competing interests:** The authors declare that they have no conflict of interest. **Data and materials availability:** All data needed to evaluate the conclusions in the paper are present in the paper and/or the Supplementary Materials. Additional data related to this paper can be requested from the authors. Split for many samples is available at the Geological Museum of Lausanne, Switzerland.

Submitted 22 November 2016

Accepted 26 February 2018

Published 11 April 2018

10.1126/sciadv.1602921

Citation: F. Zhang, S. J. Romaniello, T. J. Algeo, K. V. Lau, M. E. Clapham, S. Richoz, A. D. Herrmann, H. Smith, M. Horacek, A. D. Anbar, Multiple episodes of extensive marine anoxia linked to global warming and continental weathering following the latest Permian mass extinction. *Sci. Adv.* **4**, e1602921 (2018).

Multiple episodes of extensive marine anoxia linked to global warming and continental weathering following the latest Permian mass extinction

Feifei Zhang, Stephen J. Romaniello, Thomas J. Algeo, Kimberly V. Lau, Matthew E. Clapham, Sylvain Richoz, Achim D. Herrmann, Harrison Smith, Micha Horacek and Ariel D. Anbar

Sci Adv 4 (4), e1602921.
DOI: 10.1126/sciadv.1602921

ARTICLE TOOLS

<http://advances.sciencemag.org/content/4/4/e1602921>

SUPPLEMENTARY MATERIALS

<http://advances.sciencemag.org/content/suppl/2018/04/09/4.4.e1602921.DC1>

REFERENCES

This article cites 107 articles, 38 of which you can access for free
<http://advances.sciencemag.org/content/4/4/e1602921#BIBL>

PERMISSIONS

<http://www.sciencemag.org/help/reprints-and-permissions>

Use of this article is subject to the [Terms of Service](#)

Science Advances (ISSN 2375-2548) is published by the American Association for the Advancement of Science, 1200 New York Avenue NW, Washington, DC 20005. 2017 © The Authors, some rights reserved; exclusive licensee American Association for the Advancement of Science. No claim to original U.S. Government Works. The title *Science Advances* is a registered trademark of AAAS.